William Krakow

Computer Simulation of High-Resolution Electron Micrographs Using Dynamical Electron Scattering

A system of computer programs has been implemented that calculates both high-resolution images and diffraction patterns of generalized objects for the conventional transmission electron microscope. Multi-slice dynamical electron scattering of $256 \times 256 = 65$ 536 beams is incorporated into these programs, which allows Bragg reflections and the diffuse scattering contributions between these reflections to be included in the computations. Images can therefore be obtained from imperfect crystalline structures and for disordered objects such as amorphous materials. Both bright- and dark-field images are obtained with this system in either the axial or tilted-beam imaging modes. Examples of surface effects in Au crystals, the [111] split Crowdion interstitial in tungsten, and an amorphous Fe film model are considered in the context of dynamical electron scattering.

Introduction

Under favorable imaging conditions, the conventional transmission electron microscope is capable of resolving point resolutions approaching 3 Å and line resolutions considerably less than 2 Å (the unit Å, used throughout this paper, is equivalent to the SI metric 0.1 nm). A wide range of materials and objects have been studied at or near these resolutions, including organometallic molecules containing heavy atoms [1, 2], amorphous materials [3-7], perfect crystalline structures [8, 9], crystals containing small voids [10] and point defects [11-13], and some extended defects [14, 15]. While the list is certainly more extensive than indicated here, most of the above work and other subsequent studies have resorted to image modeling by the computer to interpret the phase contrast micrographs in all but the most simple and apparent cases. By knowing the appropriate electron optical parameters as well as the specimen orientation, it is possible in theory to closely approximate an electron micrograph of any object. This statement is made with some caution, however, since most of the computer simulations do not use the appropriate electron-scattering formalism or have limited capability in computing the effect of the electron microscope on the transmitted and scattered waves emanating from the specimens.

Basically, most image computations use the weak phase object (WPO) scattering approximation, where single scattering is used and all the atoms are considered to lie in a single object plane. This is a good approximation for calculations of single-atom images of the type shown by Hashimoto et al. [1] and for organometallic molecules shown by Krakow [16]. However, for amorphous films more than a few monolayers thick, and where dynamical or multiple electron scattering can occur, the weak phase object approximation will not be appropriate; for example, Kenaya et al. [17], Graczyk and Chaudhari [6], and Krivanek and Howie [4]. In these cases, there would not only be the problem of multiple electron scattering but also that of projection of object features onto a single image plane. These problems preclude any quantitative identification of image features or measurement of accurate diffraction intensities.

The same arguments about weak phase objects apply to crystalline materials, where the dynamical scattering can also cause severe problems. What appear to be exceptions to this rule, where single scattering gives good approximations, are as follows: 1) the observations on small holes in graphite films by Iijima [10], where the

Copyright 1981 by International Business Machines Corporation. Copying is permitted without payment of royalty provided that (1) each reproduction is done without alteration and (2) the *Journal* reference and IBM copyright notice are included on the first page. The title and abstract may be used without further permission in computer-based and other information-service systems. Permission to *republish* other excerpts should be obtained from the Editor.

graphite lattice is at most a few tens of atomic layers thick; 2) the observations of crystalline (001) Au surfaces [18], where one is dealing with atoms of Au within one unit cell of the bounding surface; and 3) the contrast expected from the diffuse elastic scattering of displaced atoms in a crystalline lattice that shows intensities in agreement with computer calculations [12, 13]. It must be pointed out that the above results do not consider any depth to the crystal; i.e., all features are contained in a single plane. This means, for example, that the image calculations of holes in (1) do not take into account the thickness of the whole film and only a fraction of the total crystalline thickness is considered. For surface features mentioned in (2), only one surface is evaluated; thus top and bottom features have not been fully considered. For (3) only the diffuse scattering produced by the direct beam was evaluated; therefore the contributions of Bragg scattering to the diffuse scattering and diffuse-diffuse scattering have not been included. Although the above three examples give good quantitative agreement with experiment, the diffraction intensities could be in considerable error.

To date, dynamical multi-slice electron diffraction theory has been applied to the calculation of lattice images of small crystalline defect structures by Cowley and Fields [19, 20] and by O'Keefe and Iijima [14]. By restricting the number of beams or Fourier coefficients to manageable numbers (≈4000 beams), calculations could be performed at the rate of seven minutes per slice, which is exceedingly slow computationally. The film thickness considered was only 19 Å, which, even for heavy tungsten oxides, is barely in the dynamical regime. By further restricting the number of beams to 496 components and severely limiting the size of the strain field and the real and reciprocal space-sampling intervals [20], the slice calculations could be extended to a crystal a few hundred Å thick. These results, however, have apparently used large slice-thickness values of 10-15 Å to accommodate an extended strain field, which for the Au interstitial case would severely limit the accuracy of the diffraction and image calculations at 100 kV. It is apparent that the computational procedures of the above-mentioned studies are very restricted in their use and that objects which deviate from the simplest cases of ordered crystalline structures cannot be considered efficiently.

Because of the constraints mentioned above, the purpose of this paper is to describe a system of computer programs that can efficiently calculate electron microscope images and diffraction patterns for multi-slice dynamical electron scattering. The number of beams, as well as the number of slices, is not as restricted as in earlier work on this subject. Also, one need not limit the real

space or reciprocal space dimensions as severely. The computer programs are designed to avoid duplication of computational procedures and excessive I/O operations that consume valuable CPU time. The versatility of these programs is shown by several examples, which include surface topography in crystals, point defect configurations with strain fields, amorphous materials, and extended defects in crystals.

Diffraction and image theory

• Image intensity

The theory of bright- and dark-field image formation in the conventional microscope has been presented previously for weak phase objects under tilted beam illumination for both elastic and inelastic scattering [12, 16]. Only a brief outline of the important aspects of the theory (which has been modified for dynamical electron scattering) is included here.

For an inclined plane wave reaching the specimen, the complex amplitude of the wave disturbance in the range plane at some point $\tilde{r}_i = (x_i, y_i)$ can be written as

$$\psi_{\mathrm{T}}(x_{i}, y_{i}) = \frac{1}{\lambda} \int \psi_{n}(\tilde{\eta}) P(|\tilde{\eta}|) \exp\left(\frac{2\pi i}{\lambda} \tilde{\eta} \cdot \tilde{r}_{i}\right) d\tilde{\eta}$$

$$= \frac{1}{\lambda} \mathcal{F}^{-1} \{\psi_{n}(\tilde{\eta}) P(|\tilde{\eta}|)\}, \qquad (1)$$

where \mathscr{F}^{-1} is the inverse Fourier transformation operation. The image plane intensity, in the coherent imaging mode, is the square modulus of this complex amplitude $|\psi_T|^2$. The angular wave distribution emerging from the bottom of the object $\psi_n(\bar{\eta})$ requires a more detailed discussion, which is given in the next section. The vector variable $\hat{\eta}$ is given by the relation

$$\bar{\eta} = \bar{\alpha} + \bar{\beta},\tag{2}$$

which defines the angular position of the wave with respect to the microscope optic axes and where $\bar{\alpha}$ is the scattering angle with respect to the direct beam $\bar{\beta}$ (see Fig. 1). In this paper it is assumed that the incident beam is spatially coherent and that the electrons are monoenergetic; *i.e.*, there is no energy spread due to the electron source. The combined effects of spherical aberration and defocus of the objective lens, as well as the diffraction limit (objective aperture limit), are contained in the pupil function term of Eq. (1):

$$P(|\bar{\eta}|) = A(|\bar{\eta}|) \exp\left[-i\gamma(|\bar{\eta}|)\right]. \tag{3}$$

Only that portion of the total wave front which falls within the objective aperture, which is centered on the optic axis, is transmitted to the image plane. This condition is expressed by aperture function $A(|\bar{\eta}|)$, contained in the pupil function, which is defined as

59

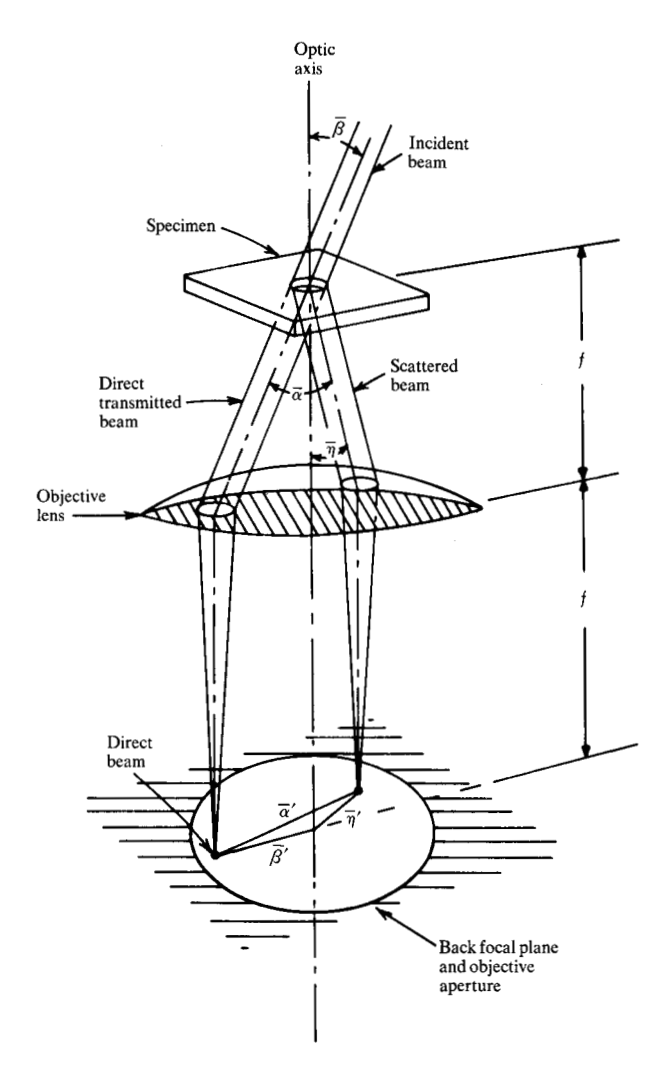


Figure 1 Ray diagram of the microscope geometry for tilted beam imaging. $\bar{\beta}$ is the beam tilt angle, $\bar{\alpha}$ the scattering angle with respect to the direct transmitted beam, and $\bar{\eta}$ the scattering angle with respect to the optic axis. Here vectors are used to specify both magnitude and direction. The coordinates in the back focal plane $(\bar{\alpha}', \bar{\beta}', \bar{\eta}')$ are obtained by multiplying the angles $(\bar{\alpha}, \bar{\beta}, \bar{\eta})$ by the focal length of the objective lens.

$$A(|\bar{\eta}|) = 1 \text{ for } |\bar{\eta}| < R$$

$$= 0 \text{ for } |\bar{\eta}| \ge R,$$
(4)

where R is the aperture radius in angular coordinates. Here a bright-field image is obtained for $|\bar{\beta}| < R$ and a dark-field image for $|\bar{\beta}| \ge R$. The pupil function also contains the phase shift γ , introduced by the objective lens:

$$\gamma(|\bar{\eta}|) = \frac{2\pi}{\lambda} \left(\frac{1}{4} C_s |\bar{\eta}|^4 - \frac{1}{2} \Delta f |\bar{\eta}|^2 \right), \tag{5}$$

where C_s is the spherical aberration coefficient, Δf the defocus, and λ the electron wavelength.

The power spectrum of the image intensity is the square modulus of the Fourier transform of the image plane intensity. Filtered electron microscope images are obtained first by a Fourier transformation of the image intensity, by application of the appropriate filter function, and then by back-transformation to produce the filtered image.

• Diffraction in crystals

The form of the scattered wave emerging from the bottom of the crystal $\psi_n(\bar{\eta})$ shown in Eq. (1) requires further explanation in terms of the mathematical formalism. Essentially, the basic feasibility for multi-slice formalism has been given by Cowley and Moodie [21] and numerical evaluation methods have been summarized by Goodman and Moodie [22]. This formalism has been applied to perfect crystalline structures requiring a limited number of Bragg beams. Preliminary investigations have been applied to arrays of defects using methods of periodic continuation and superlattices of these defects [20-22]. This latter method is rather cumbersome and requires matching of boundary conditions at the edges of a real-space superlattice, which in practice cannot be achieved for many classes of objects such as amorphous materials, extended defects, and even point defects with extended strain fields. Since multi-slice computational procedures were readily available for perfect crystals, the periodic continuation method was adapted to introduce an artificial reciprocal lattice mesh between strong Bragg reflections. Here, one can sample the deviations in scattering due to a lack of order in the object. This requires careful consideration of the fineness of the mesh for the artificial lattice to include all the Fourier components used to form an image. In essence, this method is equivalent to sampling an interval of reciprocal space points fine enough to include the effects of diffuse scattering. Therefore, one need not extend the object by periodic continuation since all the information is contained in the original object if the reciprocal space scattering is sampled in fine enough intervals. This is the basis of the multi-slice formalism used in this paper. It does not assume any approximations to the scattering by omitting cross terms [20], but considers fully the interaction of the Bragg and diffuse scattering in all regions of reciprocal space (e.g., Huang scattering). It also allows a number of different defects to be included in the same field of view, which would be difficult using periodic continuation.

The multi-slice formalism presented here is for a "generalized" object and is similar to that of a perfect crystal except that reciprocal lattice vectors \bar{g} corresponding to Bragg reflections are now replaced by vectors $\bar{\eta}$ corresponding to an arbitrary reciprocal space region. These vectors can include regions between the Bragg reflections

or, in the case of an amorphous object, any reciprocal space vector. By considering discrete crystalline layers, the form of the scattering exiting from the *n*th layer is given by the recursion relation

$$\psi_n(\bar{\eta}) = [\psi_{n-1}(\bar{\eta})P_{n-1}(\bar{\eta})] * Q_n(\bar{\eta}), \tag{6}$$

where * specifies a convolution product of these complex arrays. The Fresnel propagation function P_n from the n to n+1 layer is specified by the two-dimensional distribution function

$$P_n(\bar{\eta}) = \exp(i\pi Z_n \eta^2 / \lambda), \tag{7}$$

where Z_n is the distance between the layers. (The functions here are displayed without their arguments to shorten the notation.) The scattering distribution of the object Q_n on the *n*th layer is given by the sum of a direct beam term represented by a delta function and a weak phase object scattering distribution representing the atomic potential distribution of the object,

$$Q_n(\bar{\alpha}) = \delta(\bar{\alpha}) - iF_n(\bar{\alpha})\Delta Z_n, \tag{8}$$

where ΔZ_n is the slice or layer thickness and F_n is the scattering distribution of the *n*th layer, given by

$$F_n(\bar{\alpha}) = \sum_{j}^{\text{all atoms}} f_j(\alpha) \exp\left[\frac{2\pi i}{\lambda} (\bar{\alpha} \cdot \tilde{r}_j)\right], \tag{9}$$

where f_j is the atomic scattering factor for each atom at a real space position \bar{r}_i .

For the initial layer n=1, $\psi_0 P_0$ in Eq. (6) is replaced by a delta function $\delta(\bar{\eta}-\bar{\beta})$, where $\bar{\beta}$ represents the direct beam tilt. Beam tilt need only be taken into account in this initial delta function; all future convolutions using Eq. (6) will include its effect. Of course, the propagation distance Z_n and slice thickness are also modified for beam tilt by increasing their respective distances by the reciprocal of the cosine of the beam tilt angle.

Computational procedures

The calculation of atomic images involves the use of a series of computer programs to input atomic position data and obtain a numerical solution to Eq. (1). Before the image can be obtained, however, the recursion relation of Eq. (6) is evaluated to obtain the electron wave front emerging from the object of interest.

The procedures used to calculate electron micrographs are as follows:

 Input data on atom type and coordinates are stored on files for each unique slice of atomic positions; i.e., each small but finite thickness slice is considered to lie in a single plane.

- 2. The scattering distribution of each unique layer is calculated using the WPO approximation of Eq. (9), where the atomic scattering factors are calculated from analytical functions. These complex scattered wave distributions are then permanently stored for future use in the multi-slice diffraction computations.
- The delta function representing the direct beam inclination is calculated and archived for future use.
- 4. For a specified object distribution, a menu of scattering distribution types is created which consists of a finite number of weak phase object slices, the separation between slices Z_n , and the slice thickness ΔZ_n .
- 5. The propagating function of Eq. (7) is calculated for unity thickness and stored for future use.
- 6. The solution of the *n*th recursion relation in Eq. (6) is then obtained. Here, the menu of scattering distributions must begin with the direct beam intensity distribution function and successive scattering distributions from succeeding slices are called by the menu. The scattering distribution need not be acquired again if it is identical to that of the preceding layer. The same is true of the propagation function if the distance between layers is constant. In addition to these time-saving features, all convolutions are performed using fast Fourier transform (FFT) algorithms. The emerging wave function can then be used to calculate the diffraction intensity at the bottom of the crystal by obtaining its square modulus.
- 7. Image intensity computations are then performed using the various microscope input parameters $(C_s, \Delta f, \lambda, R, \cdot \cdot \cdot)$ in Eq. (1).
- 8. Image intensities are then stored in an array where the contrast is stretched to the maximum available depending on the particular display mode used. Typical hard copy is obtained on plain paper using font characters resolving 140 distinct grey levels of intensity.

For most of the work presented here a total of 256×256 picture elements were used at picture element resolutions of 0.5 or 0.25 Å, which are well beyond the resolution limits achieved in practice in any conventional microscope at 100 kV. In fact, the maximum resolution in any computed image, which will soon be demonstrated, is 2 Å. This condition is sufficient to include enough image points to avoid biasing effects in computed images.

The computation times for the multi-slice diffraction computations are ≈ 13 s of CPU time per slice on an IBM/370 processor for the 256 \times 256 complex arrays. It is therefore possible to compute diffraction intensities of an object several hundred angstroms thick at a slice thickness of a few angstroms in perhaps ten minutes. This represents an increase of approximately 400 to 500 times in computational speed over previous numerical evaluation

procedures and computer systems in [14, 19, 20], where numbers are stated explicitly. It is believed that these differences are due partially to the use of two-dimensional FFT techniques now being incorporated into several computer systems or minicomputers that are compatible with IBM software. It has now been recognized that Ishizuka and Uyeda [23] have made use of the FFT routines for up to 8192 Bragg beams. This number of beams is necessary for accurate diffraction intensities for a complex structure like chlorinated Cu-phthalocyanine. However, their method considers only Bragg beams for a perfectcrystal structure and does not consider deviations from periodic structure that produce diffuse scattering between the Bragg reflections. Also, no timing data is given for their multi-slice calculations; therefore, it is difficult to compare their results with the examples given in this paper or to compare their computational times with those presented here.

It is also important to point out that most multi-slice computations using a large number of beams consider the scattering distributions for each slice to be identical, thus reducing or eliminating I/O operations on the computer. The point of this paper is that this approach cannot be used for generalized objects, since the layers or slices are often nonrepeating. As specified in the calculation procedure item (4), a menu of different scattering distributions are created that are not unique.

It must also be pointed out that if one wishes to consider a "generalized" object, one must make a compromise between the number of Bragg reflections and the total number of reciprocal space points evaluated. For example, there are 169 Bragg beams but 256×256 reciprocal space points evaluated for the [111] split Crowdion in tungsten. However, including these regions of reciprocal space away from the Bragg reflections permits diffraction calculations dealing with crystal size and shape effects, grain boundary diffraction effects, etc.

Image computational speeds are also typically very fast and use FFT techniques. Depending on the size of the objective aperture, the total CPU time varies between 15 and 60 s, including display CPU time. Image filtration and calculation of the power spectrum of an image are comparable to the image computational time. It is not unrealistic to perform 20 or 30 image computations per day; this is comparable to the output expected from experimental high-resolution electron microscope experiments.

At present, the image computations presented here do not include the effects of incident-beam divergence (partial coherence) and thermal diffuse scattering, and assume only elastic scattering processes. It should be emphasized

that the increased time required to do a realistic simulation with multiple scattering, compared with the WPO method, involves not only a factor corresponding to the number of slices but also a factor corresponding to the number of plane-wave components required to represent the actual incident beam's spatial coherence. This is usually very simply incorporated in the image intensity calculation for a weak phase object by modifying the microscope transfer function (e.g., see Krakow and Siegel [24]). For dynamical scattering, this would require that separate image computations be performed for each beam direction, and image intensities would then be summed. This is, at present, an intractable problem involving a several-hundred-fold increase in computer power or CPU time, and would tax the limits of the largest computer mainframe.

Image computation results

The intent of these computer modeling experiments is to match images of real electron micrographs and predict the types of images one might expect under specific microscope conditions where single scattering is not valid. Here, a widely diverse class of objects ranging from crystalline to amorphous demonstrate the versatility of the computer program system.

• Crystalline (001) Au films and surface structure

The surface structure of (001) Au films has been under investigation using high-resolution imaging by this author during the past few years [18, 25] and it is apparent that, in addition to the bulk lattice periodicity of 2.03 Å corresponding to {200} bulk reflections, larger periodicities exist from a surface lattice of partially filled unit cells. The surface period is 2.86 Å and corresponds to mixed Miller indices of {110} reflections, which are forbidden in the bulk structure.

Here, a model of the (001) surface of Au was constructed with the aid of the computer by using a primitive two-dimensional lattice periodicity of 2.86 Å. A fractional occupancy criterion was chosen arbitrarily such that of all atomic sites available in a perfect face-centered-cubic (fcc) lattice only 75% could be filled. The first layer was filled using a random number generator to assign either occupied or empty sites for the atom positions. The next layer was somewhat more difficult to construct since the stacking sequence along the [001] direction is of the ABABAB. . . type, where the B layers are shifted by an amount $a_0/2$ in the [100] and [010] directions. Here again, a fractional occupancy of 75% was assumed with the additional criterion applied that each one of these atoms must be supported by four atoms from the layer below it. If this criterion was not met, the atom was assumed to sit in an unstable position and hence was not included in the model. The same procedure was repeated for successive layers until the number of atoms which could exist in a stable configuration was exhausted, i.e., the surface terminated.

The above procedure can be applied to either top or bottom surfaces of a thin film where a change in the random number generator will produce a different atomic arrangement of surface atoms. The bulk lattice is generated simply by filling all sites in a 40 \times 40-atom array (114 \times 114-Å area) and shifting the next layer by $a_0/2$ along the [100] and [010] directions to form a layer of a perfect fcc lattice one unit cell thick with a lattice constant of 4.06 Å.

Displayed in Fig. 2 is a model of the top surface of Au, which consists of three partially filled monolayers displayed in projection. The layers contain 1189, 337, and 22 atoms, corresponding respectively to 74, 22, and 1.5 percent of the possible atomic sites. Figure 3(a) is the computed diffraction pattern intensity using Eq. (9) from the layer containing 337 atoms, while Fig. 3(b) shows the diffraction pattern of the perfect fcc lattice. It is interesting to note that the 337-atom-lattice diffraction pattern contains both the unmixed indexed reflections characteristic of the bulk lattice and mixed indexed reflections, as well as a considerable amount of scattered intensity away from the Bragg spots. This indicates considerable disorder in the surface arrangement, i.e., missing atoms. The perfect crystal pattern in Fig. 3(b) shows neither these forbidden reflections nor diffuse scattering.

Using the recursion relation of Eq. (6), a number of different diffraction patterns have been obtained using top surface layers, bulk crystals, and bottom surface layers. Film thicknesses up to 300 Å have been considered, of which the top 6 Å and bottom 6 Å were the surface layers described above. For a wide range of thicknesses, the diffraction patterns are similar to those of Fig. 3(b) and there are additional weak reflections located at the centers of the squares defined by the matrix or bulk lattice reflections. These reflections can be seen if the image display of the diffraction data is properly scaled; however, Fresnel and Fraunhoffer diffraction effects from the edges of the model are also visible if too many decades of intensity are included. This problem could be alleviated by constructing a model which has a circular boundary instead of the square shape currently employed.

Examples of computer-generated images of the (001) Au film with one rough surface are shown in Fig. 4. Figure 4(a) shows the effect of using tilted beam illumination such that the (200) bulk reflection and the direct beam are equally inclined to the optic axes of the microscope. The microscope parameters used were $\beta = 0.0091$ radians, R

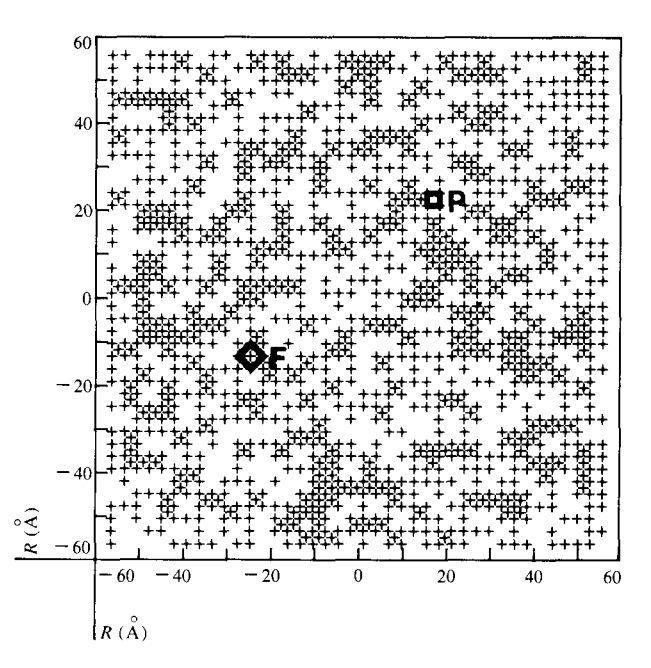


Figure 2 Au atom position model for one (001) surface using a 75% occupancy criterion. Here three layers of 1189, 337 and 22 atoms are superimposed. The primitive unit cell of the surface is indicated by the letter P, while the bulk fcc lattice is indicated by the letter F.

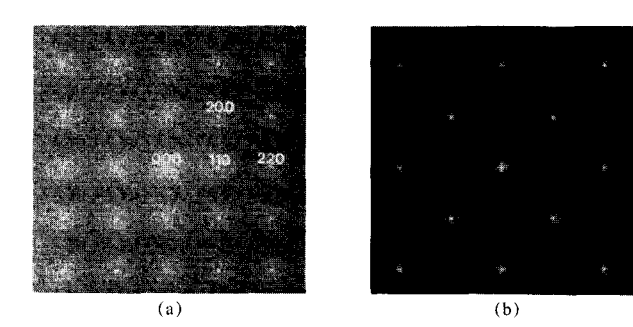
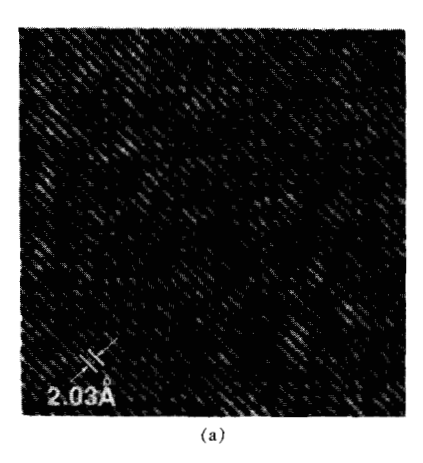
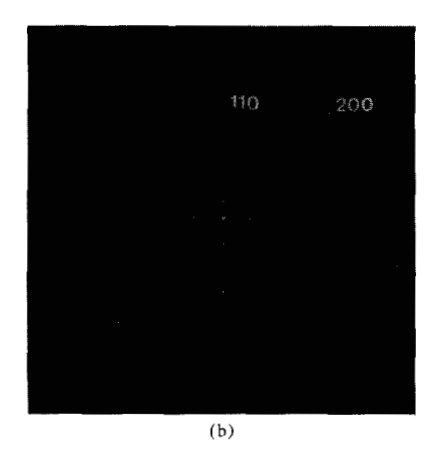


Figure 3 Computed (001) diffraction pattern intensities (a) from a 337-atom layer of the surface; (b) from a layer containing the perfect fcc unit cell structure. Note that the forbidden reflections of mixed indices in (a) are not present in (b). The reciprocal space display is $\approx 2 \ \text{Å}^{-1}/\text{side}$.

= 0.015 radians, $\Delta f = 850 \text{ Å}$, $\lambda = 27.02 \text{ Å}^{-1}$. Here the 2.03-Å lattice fringes characteristic of the bulk structure are visible and the power spectrum of this image, which is characteristic of a tilted beam image, is displayed in Fig. 4(b). Since the (200) bulk lattice fringes occur at angular distance in the power spectrum of 0.018 radians, a circular filter function can be applied to image (a) which allows





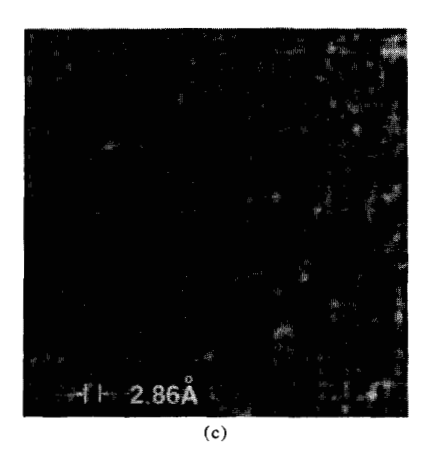
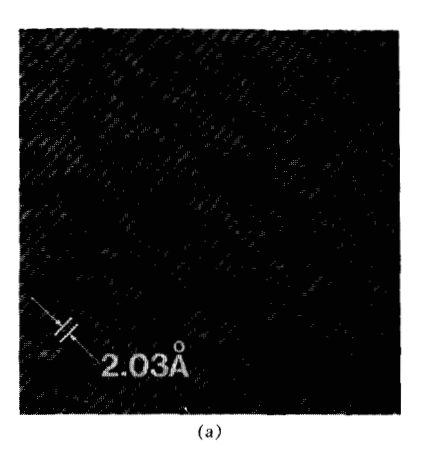
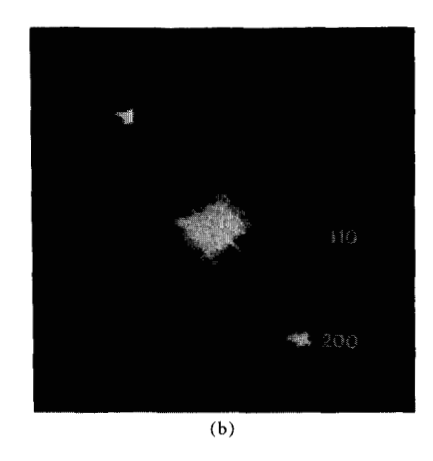


Figure 4 Computer-generated tilted beam bright-field images of one Au surface and the bulk lattice: (a) image including the (002) bulk lattice reflection and two {110} surface reflections; (b) power spectrum of image (a); (c) surface lattice image showing 2.86-Å periodicities by removing the bulk lattice image of (a).





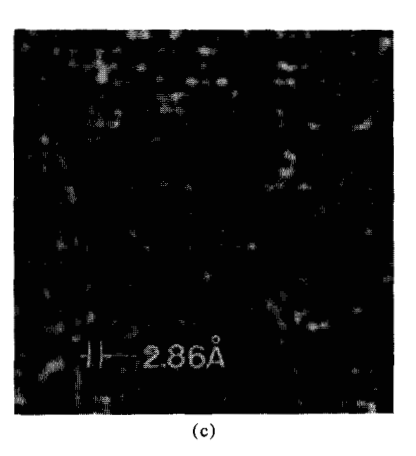


Figure 5 Experimental micrographs of (a) (200) bulk lattice fringes, (b) power spectrum of image (a), (c) surface lattice image from the {110} reflections.

only the $\{110\}$ reflections to be imaged. For an angular radius of R=0.015 radians, the corresponding filtered image is displayed in Fig. 4(c) and clearly shows the 2.86-Å lattice periodicity. The filtered image is equivalent to obtaining an image where the microscope objective aperture is smaller than the diffraction limit necessary to resolve the (200) bulk lattice periodicity. A large objective aperture can be employed if the sample is appropriately tilted to eliminate the bulk lattice $\{200\}$ periodicities $\{i.e., say a tilt about a [220] axis).$

In order to show the exactness of the computer modeling calculations, real experimental micrographs of a (001) Au film are displayed in Fig. 5. Figure 5(a) shows the (200) bulk lattice periodicity and Fig. 5(b) is its corresponding power spectrum. Figure 5(c) is an image of the (001) surface lattice obtained by filtering out the bulk lattice periodicities. It can be seen that excellent agreement between experimental micrographs and the computer-calculated images has been achieved for both bulk and surface lattice structures.

◆ Point defects—[111] split Crowdion interstitial in tungsten

In order to demonstrate that electron microscope images of localized disorder in bulk crystals can be computed for dynamical electron scattering, the [111] split Crowdion interstitial will be considered here. A unit cell model of

this defect is shown in Fig. 6. Up to this time all the prior dynamical computational procedures (e.g., Ref. [20]) considered a weak phase object approximation by taking the atom to lie in a single scattering plane. This implies that the three-dimensional effect of the strain field was totally negated.

Here examples will be shown of propagation of electron wavefronts through several slices of crystalline material where differing strain-field distribution and hence diffuse elastic scattering distributions are obtained depending on the distance from the defect core. It is important to emphasize that in a real experimental situation the visualization of point defects is still somewhat tentative, since no one has worked with a system where the strainfield distribution is well known. Here, the intent is to show that, given a model of the atomic displacements of a point defect, one can calculate using dynamical theory the image intensity produced by the scattering from a defect in a crystal. Furthermore, one can predict the intensity and image features expected in real electron micrographs.

The lattice model for the [111] split Crowdion interstitial was obtained by first constructing via the computer a perfect body-centered-cubic (bcc) crystalline lattice. Here, each lattice layer consisted of a planar arrangement of atoms with a square primitive two-dimensional lattice with a d-spacing of 3.16 Å. Thus adjacent layers could be constructed by shifting the lattice by 1/2 the d-spacing along the three $\langle 100 \rangle$ directions simultaneously. The lateral extent of the model corresponded to 15×15 atoms per layer, which is equivalent to a crystal dimension of ≈ 50 Å on a side.

The defect strain field can be included in the perfect lattice by using the tabulated values of Benedek and Ho [26]. In this case the number of atoms considered for this strain field consisted of 182 atoms where each atom was assigned an ideal lattice position site in terms of integer numbers representing half unit cell parameters (a,b,c). If these integer numbers matched the perfect bcc lattice integers, the strain-field displacement was added to the atom positions vectorially. Different heights of the defect were assigned different position designations or negative integer numbers c, so that different slices through the crystals contained different strain-field contributions depending on the level of the defect sampled. Figure 7 is a projected strain-field map of the split Crowdion with directions of the displacements from the ideal lattice positions. Here the correct magnitudes of the displacement vectors are not shown because they are at most a few hundredths of an angstrom, except for the core atoms (see Ref. [27]). Furthermore, the strain field is displayed

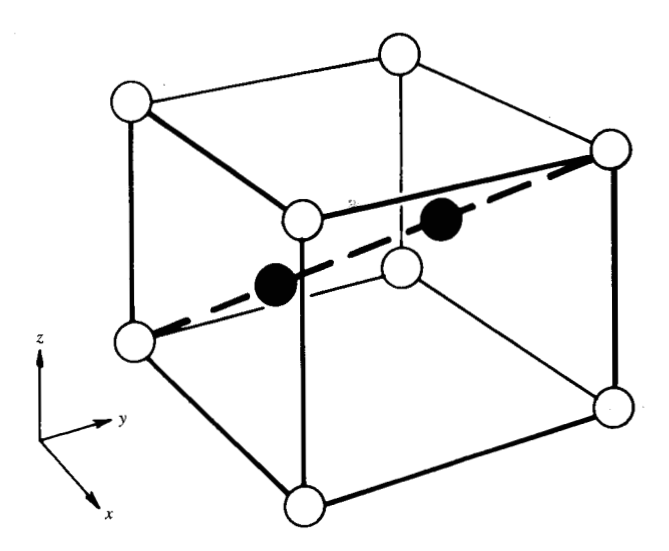


Figure 6 Schematic diagram of the unit cell containing a [111] split Crowdion interstitial in tungsten. The black dots show the location of the interstitial and displaced W atoms where the latter occupied the lattice site at the center of the cell in a perfect crystal

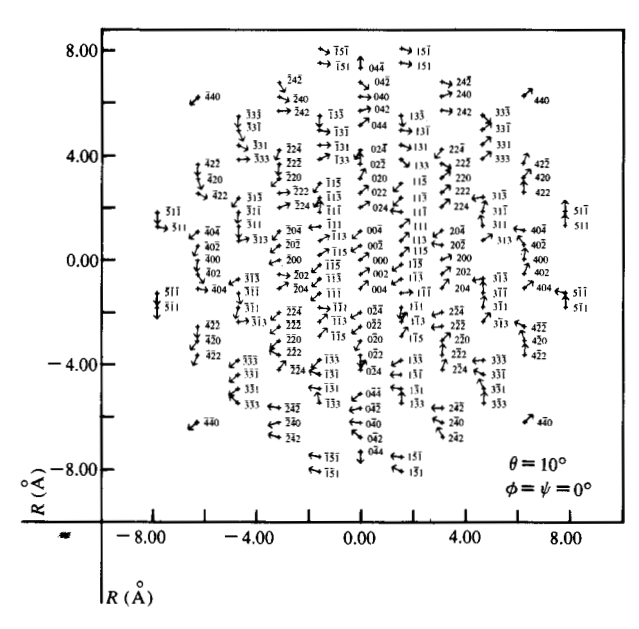
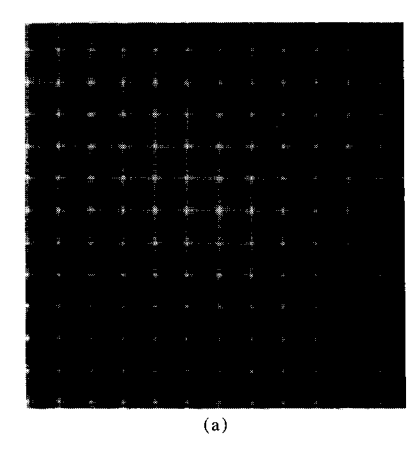
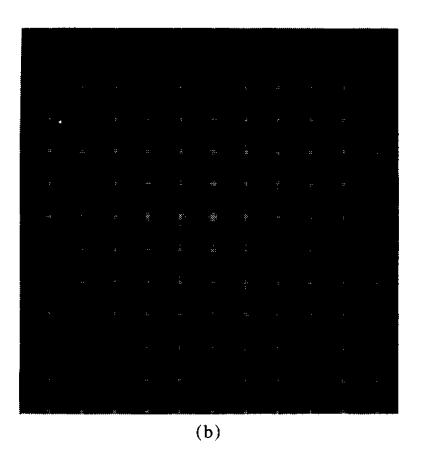


Figure 7 Map of the atom displacements (strain field) for a [111] split Crowdion interstitial in tungsten (182 atoms) when projected onto the microscope image plane. Here the crystal is tilted by 10° about a [100] direction to allow atoms at different depths to be visible.

with a 10° tilt to allow atoms at different depths to be clearly displayed. This is a rotation about the abscissa of 10° or in terms of Eulers angles $\theta = 10^{\circ}$, $\phi = \psi = 0^{\circ}$ (see Ref. [28]).





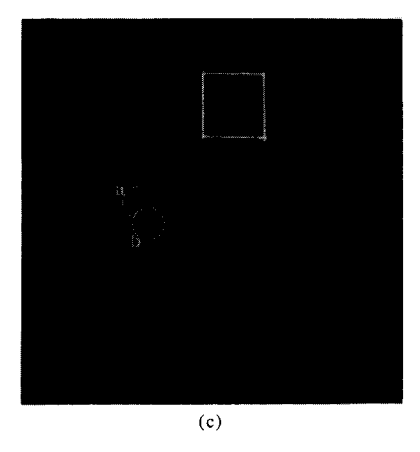
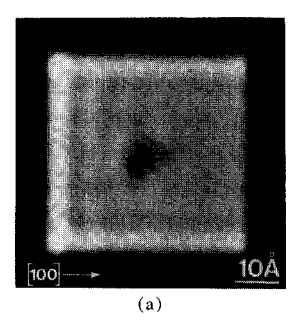


Figure 8 Diffraction patterns of the [111] split Crowdion defect in tungsten for a (001) orientation. (a) and (b) are weak phase object patterns from single layers containing strain-field distributions unique to each layer. Note the diffuse scattering and the primitive lattice periodicity. (c) is the multi-slice diffraction pattern of 22 layers containing the whole Crowdion defect. Note that the reciprocal lattice pattern here is fcc, which is the reciprocal space representation of a bcc crystal. The display distance of the images is 4 Å^{-1} /side.



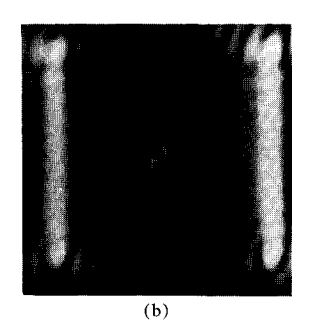


Figure 9 Dynamical diffraction dark-field images of the [111] split Crowdion in tungsten, (a) from a (002) matrix reflection, (b) from the diffuse scattering region near the (002) reflection. See Fig. 8(c) for the location and size of the objective aperture.

The computed diffraction patterns using Eq. 9 for weak phase object layers of the bcc crystal containing the Crowdion defect are shown in Figs. 8(a) and (b). Images (a) and (b) were derived, respectively, from atoms with position designations (a,b,1) and (a,b,0). The latter corresponds to the layer through the center of the defect and includes the (0,0,0) position atom (see Fig. 6). Here Fig. 8(b) was constructed from one more atom than the 15 \times 15 = 225 required for the other layers to allow accommodation of the extra interstitial atom. In Figs. 8(a) and (b), the images are displayed with eight decades of intensity to show the Bragg scattering and the background diffuse elastic scattering due to the strain field. The ringing along the line connecting the diffraction spots is due to edge diffraction effects, which unfortunately occur because the original bcc model has its boundaries perpendicular to these directions. These edge effects can be discounted in images and are of no concern except that they somewhat mask the Bragg scattering. Note that both diffraction patterns show a primitive square lattice consisting of a 13×13 array of Bragg spots. This is expected since each layer has a spacing of 3.16 Å in a primitive square lattice. It is not until multi-slicing occurs that the bcc nature of the diffraction pattern is apparent from the cumulative scattering effect of two or more adjacent layers.

The results for dynamical electron diffraction from a crystal containing the Crowdion defect for a film thickness of approximately 50 Å were obtained from the kinematic scattering distributions. Here the sequencing of layers was five layers of perfect bcc lattice one unit cell thick (i.e., two monolayers), followed by 12 layers each a monolayer thick and containing unique strain-field distributions. This was then followed by five layers of a perfect bcc lattice one unit cell thick. The diffraction pattern for multi-slicing is shown in Fig. 8(c). Here it can be seen that the reciprocal space (001) projection is an fcc unit cell, which is to be expected when a bcc real lattice is transformed to reciprocal space. A reciprocal lattice unit cell has been boxed in to make observation easier. Note that the diffuse scattering is not visible because too few decades of intensity were included. The curvature of the Ewald sphere is apparent for this pattern where the incident beam intensity is along the [001] zone.

The results of image computations from the dynamical diffraction pattern are displayed in Fig. 9 for two cases of dark-field imaging. Here a small objective aperture was

used to avoid a lattice imaging mode. It demonstrates that images can be visualized even when the objective aperture is diffraction-limited by an angular radius of R=0.005 radians, which corresponds to a real-space resolution of ≈ 3.7 Å. Figure 9(a) represents imaging from a (002) matrix reflection, while Fig. 9(b) represents an image formed from the diffuse elastic scattering from a region adjacent to this reflection. The exact diffraction conditions from images 9(a) and (b) are displayed by small circles labeled respectively a and b in Fig. 8(c) to show the reciprocal space regions sampled. It must be reiterated that the dotted diffraction lines around each Bragg spot are of no consequence since they are produced by edge diffraction and hence do not contribute to the image in the region of the defect as evidenced by Fig. 9.

• Amorphous materials

To demonstrate the multi-slice diffraction computation of an amorphous material, a model consisting of 5390 atoms was provided from a portion of the Finney model [29], which is composed of 7928 atoms. This model has been used extensively by Graczyk and Chaudhari [6] and Chaudhari [30] to investigate the scattering properties of dense random packings of atoms and to determine whether dislocation-like defects could be supported in amorphous metallic solids. In the experiments described here the model was scaled to the nearest neighbor distance in Fe of 2.55 Å and all diffraction computations were based upon the scattering factors for this atomic species. The 5390-atom model geometry is in the form of a cylinder which is 48 Å deep and 45 Å in diameter. A view along the cylinder axis of all the atoms in projection is shown in Fig. 10. This is the orientation of the model used for electron microscope imaging and diffraction calculations where the incident beam is approximately parallel to the cylinder axis.

For the multi-slice calculation the model was divided into slices 4 Å thick along the cylinder axis. The atomic population of each slice varied in number between 420 and 455 atoms. An example of the diffraction pattern and images obtained from one of these thin slices is shown in Fig. 11. Here image (a) is the computed diffraction pattern and images (b) and (c) are images with a contrast transfer function (CTF) of unity for microscope resolutions of 1.5 and 2.5 Å, respectively. These resolutions correspond to objective aperture sizes of 0.025 and 0.015 radians, respectively, for 100-kV electrons.

The results for multi-slicing through twelve 4-Å layers of Fe are shown in Fig. 12. The diffraction pattern displayed in (a) shows an apparent broadening of the second diffuse halo over the weak phase object pattern of Fig. 11(a). Images in Figs. 12(b) and (c) are bright-field images

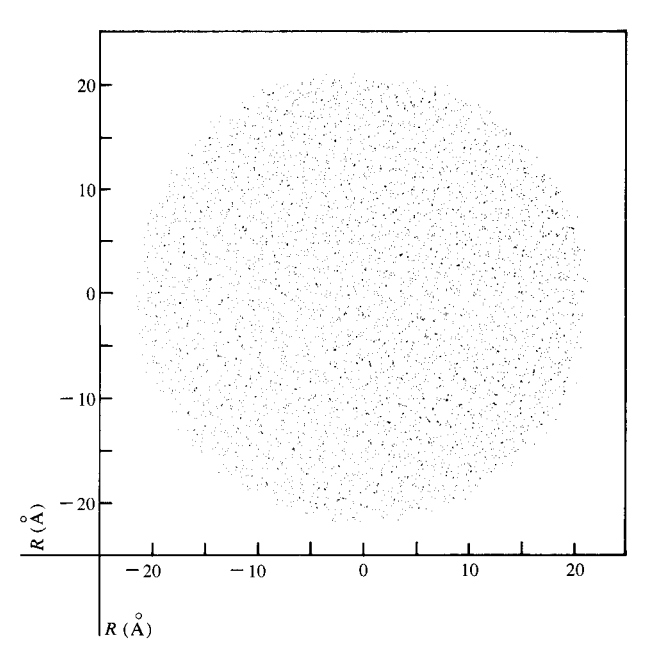
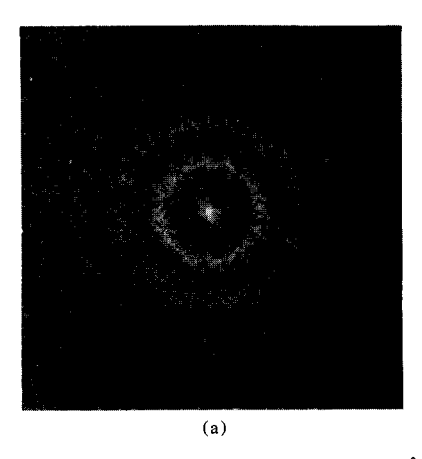
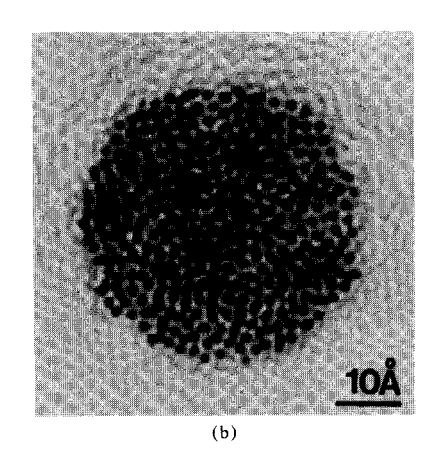


Figure 10 Atomic distribution of atoms for an amorphous solid seen in projection along the cylinder axis. Here the cylinder contains 5390 atoms and the display represents the projection of \approx 48 Å thickness.

with a CTF of unity for objective aperture sizes of 0.025 and 0.015 radians and can be compared directly to the weak phase object images of Figs. 11(b) and (c). It is interesting to note in Fig. 12(b) that there is a correspondence between the atom positions of the model and the white image features; however, here we are well beyond the point-to-point resolving power of a real 100-kV microscope. The darkened regions in Fig. 12(b) correspond to regions which are less densely populated in traversing the full thickness of the cylinder. Here, because the darkened regions do not allow precise atomic position data to be determined, only projected density variations can be obtained. This situation is considerably worsened when the microscope resolution is diminished to 2.5 Å in Fig. 12(c). Here there are poorer correlations between bright image patches and the projected density of atoms. The situation is not favorable in dark-field imaging with microscope aberrations as shown in Fig. 12(d). Here the bright fringelike patches are uncorrelated with the number density of the model. The poor agreement of the dark-field image is due to sampling of a limited region of reciprocal space, which enhances image features with spatial separations along given directions.

The apparent broadness of the diffraction pattern due to multi-slicing in the amorphous model is more easily vi-





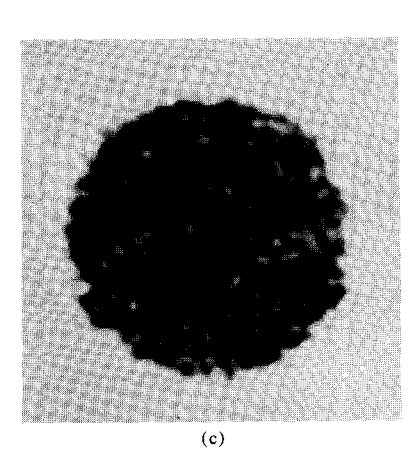
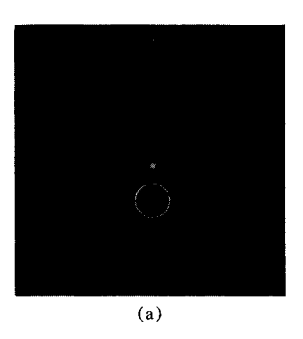
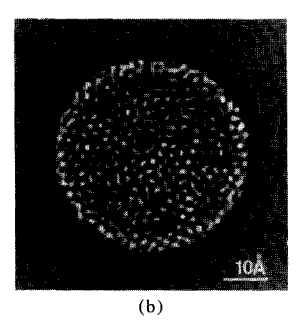
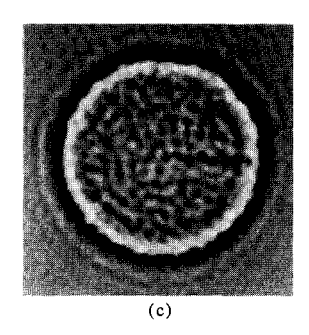


Figure 11 (a) Diffraction pattern of a 4-Å-thick slice of the amorphous model which contains 420 atoms. The display is 4 Å^{-1} /side. (b) Weak phase object bright-field image for a contrast transfer function of unity and a resolution level of 1.5 Å. (c) Same as image (b) except that the resolution is now 2.5 Å.







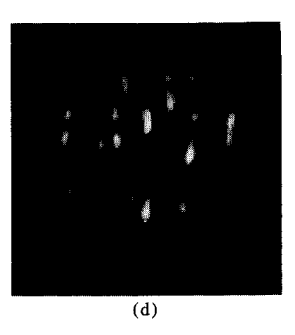


Figure 12 (a) Multi-slice diffraction pattern from the amorphous model \approx 48 Å thick. The reciprocal space display is \approx 4 Å⁻¹/side. (b) Bright-field axial illumination image obtained from pattern (a) for a resolution of 1.5 Å and a contrast transfer function of unity. (c) Same as image (b), but the resolution is now 2.5 Å. (d) Tilted beam dark-field image from the first diffraction halo as indicated in (a). The resolution level is \approx 2.1 Å. In images (b) to (d) the display size is 64 Å/side.

sualized by taking line scans of the intensity in the diffraction pattern for successive layers; see Fig. 13. Here approximately the first three decades of intensity were plotted. It is apparent that the intensity of the subsidiary maxima increases in progressing to further layers, but most important is the degradation of the sharpness of the subsidiary diffraction maxima even for a relatively thin sample. These effects will be more prominent for thicker films, which implies that obtaining radial distribution functions by electron diffraction in amorphous solids is questionable since the single scattering distributions upon which they are based are no longer valid. In view of this finding, a more critical check of the significance of multiple scattering effects in an amorphous sample is needed. The interpretation of diffraction pattern line traces at different thicknesses is somewhat confused by speckle effects. What is needed is a comparison of the same total thickness of the diffraction patterns and images, computed by multi-slice and a single large-slice equivalent to the total thickness. This comparison, however, may not have meaningful information since a single large slice would soon violate the criterion of the WPO approximation requiring that the scattering be small compared to the incident beam intensity. This problem will certainly be significant in Fe films and of greater importance in higheratomic-number amorphous materials.

Discussion and conclusion

For any detailed interpretation of electron microscope images and diffraction patterns, computer calculations of model structures are invaluable when atoms are in close proximity. In the last section a number of examples of materials with three-dimensional distributions of atoms were used to demonstrate the necessity of being able to calculate the wave distributions from different layers progressively to simulate the scattering processes occurring in a real electron microscope. In this manner one is able to investigate a priori many different classes of materials and optimize the requirements of the specific material, such as thickness and orientation, as well as optimizing the appropriate electron microscope parameters.

The examples chosen for the image computations using multi-slice theory comprise objects where localized disorder occurs. In particular, the cases of crystalline surfaces, which can be rough on an atomic scale, can be dealt with for both the top and bottom surfaces. Here it was possible to show that surface structure can be visualized and its detail separated from the bulk lattice periodicities. A second area which was considered involved point defects which have an accompanying three-dimensional strain field extending a few tens of angstroms from the defect core. This class of objects can be expanded with the present computational procedures to include extended defects existing over larger dimensions in the crystal both laterally and along the direction of propagation of the electron wave fronts. The important point to emphasize is that any defect in a crystalline material can be treated regardless of its location in depth and the extent of its strain field. Of course, an amorphous material can be regarded as a special case of a crystalline material with defects. Here the disordering applies to all the atoms in the model opposed to specific atoms, as in the case of point defects. For an amorphous material each layer will be unique, whereas the strain field of a crystalline defect will have periodic components and be bounded in depth by perfect crystalline layers.

For different objects one must therefore create a menu of slices and propagate through the specified layers. The simplest case to treat is that of a perfect crystal where each slice has the same weak phase object scattering distribution. Provided the perfect crystal has a reasonably large lateral extent, only Bragg scattering occurs. In this case there should be no diffuse scattering due to shortrange order; hence in practice it is only necessary to evaluate the regions of reciprocal space corresponding to the Bragg reflections. In other words, for perfect crystalline structures the system of programs which has been described can be simplified and the requirement of 256×256 reciprocal lattice points can be reduced considerably for this special case. As soon as any nonperiodic component is introduced, this criterion will be violated. In other words, any deviation from a perfect periodic structure requires a full reciprocal space evaluation. Even the introduction of free atoms on surfaces requires the evalua-

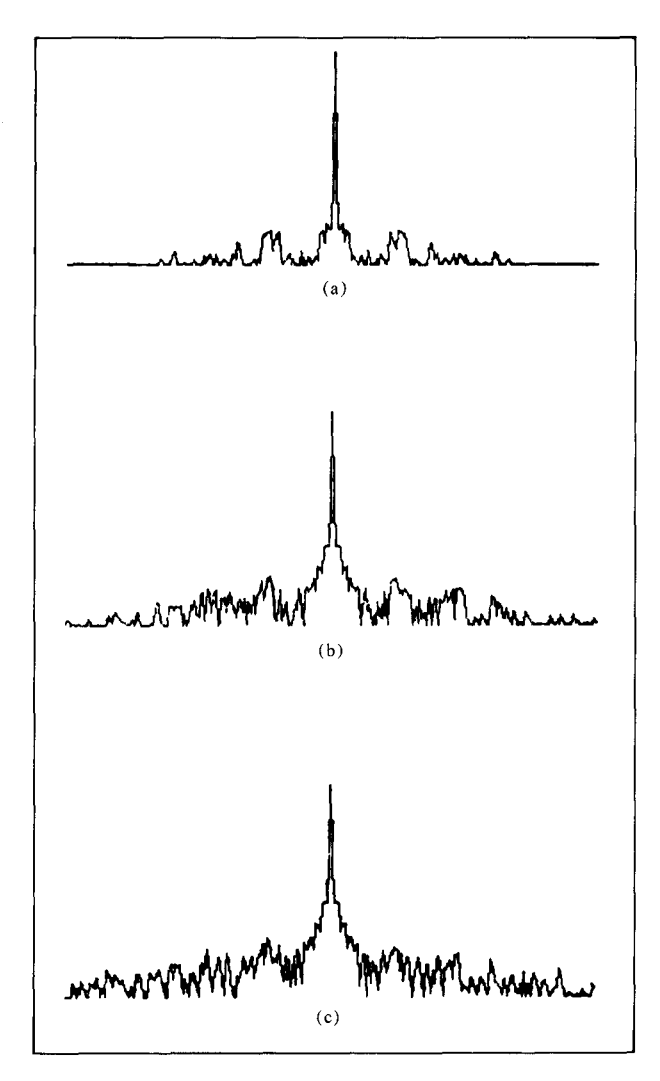


Figure 13 Line scans of the diffraction data of the amorphous model after slicing through (a) 1 layer, (b) 6 layers and (c) 12 layers. Each layer is 4 Å thick.

tion of the full range of reciprocal space. This latter topic will be considered in the numerical analysis of electron micrographs of crystalline Si containing defects and surface contaminant atoms in another publication [27].

Some further discussion of the system of computer programs is worthwhile to emphasize the computational capability of the system of computer programs for multislicing and imaging. Here, diffraction patterns are computed either for axial illumination or the tilted-beam case. In this manner it is possible to obtain bright-field images if the beam tilt is less than the objective aperture angle, or tilted dark-field images if the tilt is greater than the aperture diameter. It is also possible to include effects of astig-

matism during the image calculation and approximate the effect of partial coherence in a similar manner. Of course it is possible to consider different electron wavelengths, which demands that the weak phase object scattering be reevaluated as well as the multi-slice computations. The system of programs can compute most forms of images and diffraction patterns which one can achieve in a conventional transmission microscope. Furthermore, this system applies to a generalized object containing any atomic arrangement of atoms and is not as restrictive as earlier methods of dynamical electron diffraction.

Acknowledgments

The author wishes to thank P. Chaudhari for providing atomic position coordinates of the Finney model.

References

- H. Hashimoto, A. Kumao, K. Hino, H. Endoh, H. Yotsumoto, and A. Ono, "Visualization of Single Atoms in Molecules and Crystals by Dark Field Electron Microscopy," J. Electron Microsc. 22, 123 (1973).
- F. P. Ottensmeyer, E. E. Schmidt, and A. J. Olbrecht, "Image of a Sulfur Atom," Science 179, 175 (1973).
- A. Howie, O. L. Krivanek, and M. L. Rudee, "Interpretation of Electron Micrographs and Diffraction Patterns of Amorphous Materials," *Phil. Mag.* 27, 235 (1973).
 O. L. Krivanek and A. Howie, "Kinematical Theory of Im-
- O. L. Krivanek and A. Howie, "Kinematical Theory of Images from Polycrystalline and Random-Network Structures," J. Appl. Crystallogr. 8, 213 (1975).
- S. R. Herd and P. Chaudhari, "On the Question of Microcrystallites in Some Amorphous Materials. An Electron Microscope Investigation," Phys. Status Solidi A 26, 627 (1974).
- J. F. Graczyk and P. Chaudhari, "Scattering Properties of Dense Random Packings of Hard Spheres," Phys. Status Solidi B 75, 593 (1976).
- W. Krakow, D. G. Ast, W. Goldfarb, and B. M. Siegel, "Origin of the Fringe Structure Observed in High Resolution Bright-Field Micrographs of Amorphous Materials," *Phil. Mag.* 33, 985 (1976).
- S. Iijima, "Observation of Single and Clusters of Atoms in Bright-Field Electron Microscopy," Optik 48, 193 (1977).
- M. A. O'Keefe, "n-Beam Lattice Images. IV. Computed Two-Dimensional Images," Acta Crystallogr. A 29, 389 (1973).
- S. Iijima, "High Resolution Electron Microscopy of Phase Objects: Observation of Small Holes and Steps on Graphite Crystals," Optik 47, 437 (1977).
- A. L. J. Chang, S. L. Sass, and W. Krakow, "A High Resolution Electron Microscope Investigation of the Omega Transformation in Zr-Nb Alloys," Acta Met. 24, 29 (1976).
- W. Krakow, A. L. J. Chang, and S. L. Sass, "On the Possibility of the Direct Imaging of Point Defects in Crystals using Transmission Electron Microscopy," *Phil. Mag.* 35, 575 (1977).

- T. S. Kuan and S. L. Sass, "The Direct Imaging of a Linear Defect using Diffuse Scattering in Zr-Nb b.c.c. Solid Solutions," Phil. Mag. 36, 1473 (1977).
- M. A. O'Keefe and S. Iijima, "Calculation of Structure Images of Crystalline Defects," Proceedings of the 9th International Conference on Electron Microscopy, Toronto, Ont., 1978, vol. 1, p. 282.
- P. Rez and O. L. Krivanek, "Computer Simulation of High Resolution Images of Crystal Defects," Ref. [14], loc. cit., p. 288
- W. Krakow, "Computer Experiments for Tilted Beam Dark-Field Imaging," Ultramicrosc. 1, 203 (1976).
- K. Kenaya, T. Oikawa, K. Hojo, K. Adachi, and E. Watanabe, "Computer Simulation of Phase Contrast of Tungsten Support Film in High Resolution Electron Microscopy," J. Electron Microsc. 26, 1 (1977).
- W. Krakow, "Computer Modeling of High Resolution Transmission Microscope Images of the (001) Au Film Surface," Ultramicrosc. 4, 55 (1979).
- P. M. Fields and J. M. Cowley, "Computed Electron Microscope Images in F.C.C. Metals," Acta Crystallogr. A 34, 103 (1978).
- J. M. Cowley and P. M. Fields, Dynamical Theory for Electron Scattering from Crystal Defects and Disorder," Acta Crystallogr. A 35, 28 (1979).
- J. M. Cowley and A. F. Moodie, "The Scattering of Electrons by Atoms and Crystals. I. A New Theoretical Approach," Acta Crystallogr. 10, 609 (1957).
- P. Goodman and A. F. Moodie, "Numerical Evaluation of N-Beam Wave Functions in Electron Scattering by the Multi-slice Method," Acta Crystallogr. A 30, 280 (1974).
- K. Ishizuka and N. Uyeda, "A New Theoretical Approach to the Multislice Method," Acta Crystallogr. A 33, 740 (1977).
- W. Krakow and B. M. Siegel, "Phase Contrast in Electron Microscope Images with an Electrostatic Phase Plate," Optik 42, 245 (1975).
- W. Krakow and D. G. Ast, "Surface Structure and Surface Lattice Constant of (001) Vapor Deposited Au Films using High Resolution Transmission Electron Microscopy," Surface Sci. 58, 485 (1976).
- R. Benedek and P. S. Ho, "Lattice Statics Calculations for Interstitial Atoms in Tungsten," J. Phys. F 3, 1285 (1973).
- W. Krakow, H. Föll, and T. Tan, "Detection of Extended Interstitial Chains in Ion Damaged Silicon," Appl. Phys. Lett., in press.
- H. Goldstein, Classical Mechanics, Addison-Wesley Publishing Co., London, 1959.
- J. L. Finney, "Random Packings and the Structure of Simple Liquids. I. The Geometry of Random Close Packing," Proc. Roy. Soc. A 319, 479 (1970).
- P. Chaudhari and A. Levi, "Edge and Screw Dislocations in an Amorphous Solid," Phys. Rev. Lett. 43, 1517 (1979).

Received August 4, 1980

The author is located at the IBM Thomas J. Watson Research Center, Yorktown Heights, New York 10598.